Support Information

Chloride Regulated Cu_xO/RuCu Heterostructure Electrocatalyst towards High-Performance Li-CO_2 Battery

Liyun Ju,[a] Yanlong Wang,[a] Xijun Qu,[a] Jianwen Xu,[a] Hengyi Zhu,[a] Tao Jin,[b] Li Song,[a] Mingdao Zhang,[a] and Yachao Jin, [a]*

[a]Institute of Energy Supply Technology for High-end Equipment, Jiangsu Key Laboratory of Atmospheric Environment Monitoring and Pollution Control, Jiangsu Collaborative Innovation Center of Atmospheric Environment and Equipment Technology, School of Environmental Science and Engineering, Nanjing University of Information Science & Technology, Nanjing 210044 Jiangsu, P. R. China.

[b]Longmen Laboratory, Luoyang, Henan, 471000, China.

Email: jinyachao@nuist.edu.cn

Experimental Section

Materials preparation: Firstly, $CuCl_2 \cdot 2H_2O$ was dissolved in deionized water, and then PVP, NaOH and ascorbic acid were added to react in water bath at 40 ℃. After the completion of the reaction, the Cu_2O catalyst was obtained by centrifugal cleaning and freeze-drying. In order to modify the Cu_2O catalyst, the Cu_2O catalyst was ultrasonically dissolved in ethanol and hydrothermally reacted at 120 ℃ for 10 h by adding $RuCl_3 \cdot 3H_2O$. The modified catalyst was obtained by centrifugal cleaning and freeze-drying. By adjusting the doping amount of $RuCl_3 \cdot 3H_2O$ (0.1 mmol, 0.2 mmol, 0.3 mmol, 0.4 mmol), we named it Cu_xO-Cl/RuCu-Y (Y=1, 2, 3, 4). Since Cu_xO-Cl/RuCu-3 has the best performance, Cu_xO-Cl / RuCu-3 is denoted as Cu_xO-Cl/RuCu.

Materials characterization: X-ray diffraction phase analysis (XRD) is a technique for material structure analysis by using the diffraction effect of X-ray in crystal materials. The catalyst was qualitatively analyzed by measuring the diffraction angle position (peak position), and the catalyst was quantitatively analyzed by measuring the peak intensity of the spectral line. Scanning electron microscope (SEM) is an observation method between transmission electron microscope and optical microscope which was used to observe the surface morphology of the catalyst. Transmission electron microscopy (TEM) and high-resolution transmission electron microscopy (HR-TEM) allow us to see the finer microstructure and morphology of the catalyst. In order to further analyze the surface composition and element valence of the catalyst, XPS technology was used to analyze the catalyst. Raman spectroscopy is an efficient, non-destructive analysis technology without complex sample preparation which was used for qualitative analysis and structural identification of the catalyst.

Electrochemical measurements: The electrochemical performance of the catalyst was evaluated by assembling the button cell. 10 mg catalyst and 10 mg KB were added to the mixed solution of 1.9 ml ethanol and 100 ul nafion (10%). The catalyst loading was controlled at about 1 $mg \cdot cm^{-2}$, and the cathode electrode was obtained by vacuum drying at 80 ℃ for 12 h. The anode is metal lithium sheet with a diameter of 15.6 mm. The separator is glass fiber with a diameter of 19 mm. The electrolyte is 1 M LiTFSI /

DMSO, and the drop amount is 200 μL. The CR2032 battery shell with holes was used to assemble the battery in the glove box with H_2O < 0.01 ppm and O_2 < 0.01 ppm. The assembled battery was placed in a closed test bottle and replaced with CO_2 gas for 20 min to wait for the test which includes constant current charge-discharge testing, rate performance testing, capacity testing and CV testing.

Theoretical calculation: Density functional theory (DFT) calculations were performed carried out with the CP2K package, employing the hybrid Gaussian and plane waves (GPW) method within its QUICKSTEP module The core-valence electron separation was described by Goedecker–Teter–Hutter (GTH) pseudopotentials, while a molecularly optimized double-zeta valence plus polarization basis set (DZVP-MOLOPT-SR-GTH) was utilized for all atoms. An auxiliary plane wave basis with a cutoff energy of 500 Ry was applied to expand the electron density. Exchange and correlation effects were treated using the spin-polarized Perdew–Burke–Ernzerhof (PBE) functional under the generalized gradient approximation (GGA). The Kohn–Sham equations were solved via conventional matrix diagonalization, accelerated by the ELPA library, and electronic convergence was facilitated by Fermi–Dirac smearing with an electronic temperature of 300 K. To account for van der Waals interactions, the DFT-D3 dispersion correction scheme by Grimme et al. was incorporated. Structural relaxations were considered converged when energy and maximum force changes fell below 1.0×10^{-6} eV and 3.0×10^{-4} eV $Å^{-1}$, respectively. For electronic structure calculations, a tighter energy threshold of 1.0×10^{-8} eV was adopted. Brillouin zone sampling was performed using Monkhorst–Pack k-point meshes: 13×13×13 grid for Cu and Cu_2O unit cell, and 5×3×1 grid for Cu/Cu_2O and RuCu/Cu_2OCl heterostructures. A vacuum layer of 20 Å was added along the non-periodic direction to isolate periodic images of the slabs. The optimized lattice parameters obtained for Cu and Cu_2O was 3.66 and 4.30 Å. Thermodynamics corrections and density of states (DOS) analyses were conducted using the Shermo and Multiwfn software packages, respectively. The charge density difference was visualized using the VESTA software.

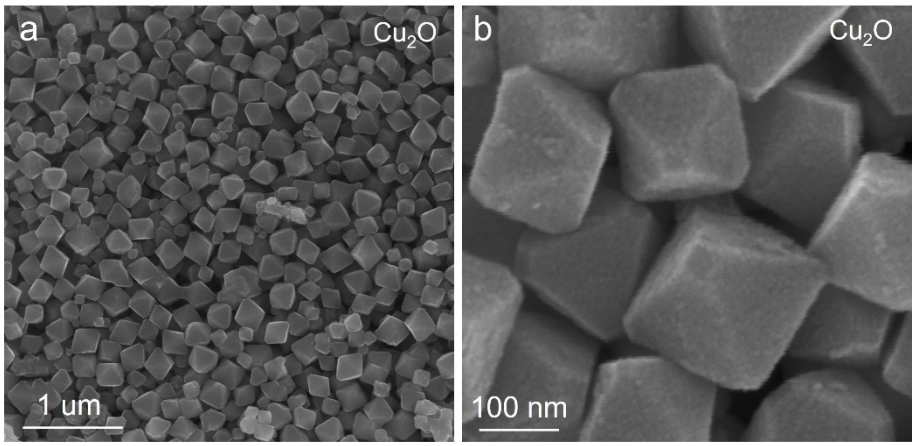

Fig. S1. SEM images of Cu_2O

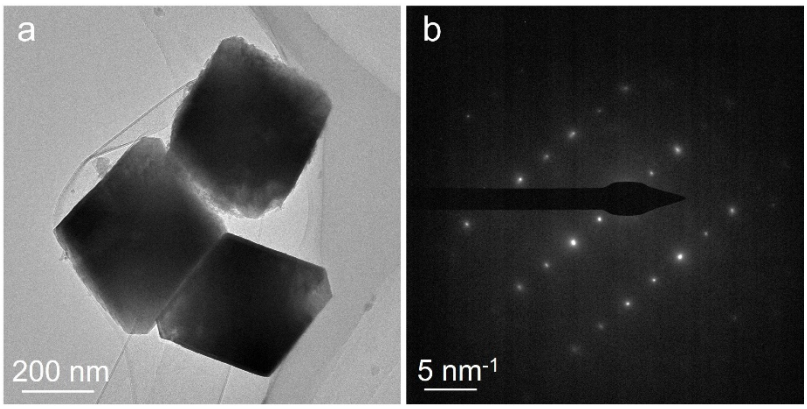

Fig. S2. (a) TEM image and (b) SAED image of Cu_2O

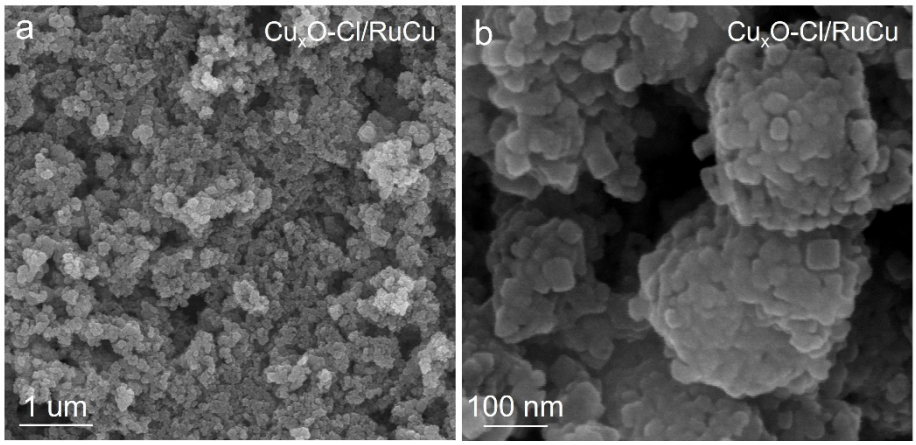

Fig. S3. SEM images of Cu_xO-Cl/RuCu

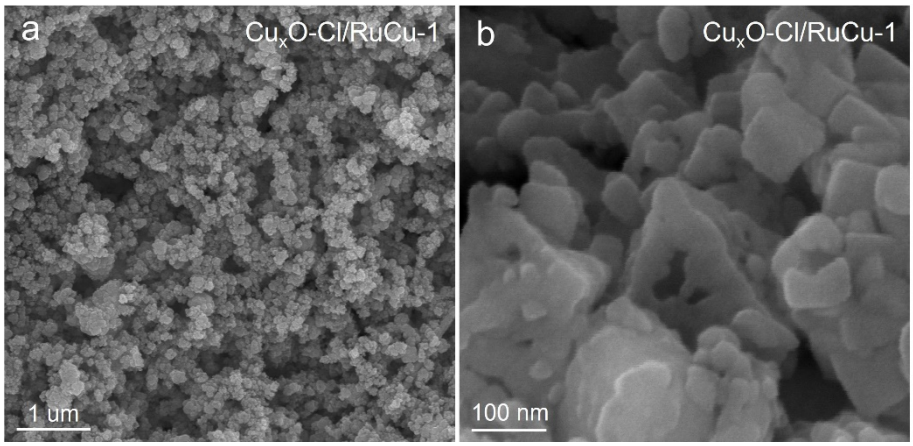

Fig. S4. SEM images of Cu_xO-Cl/RuCu-1

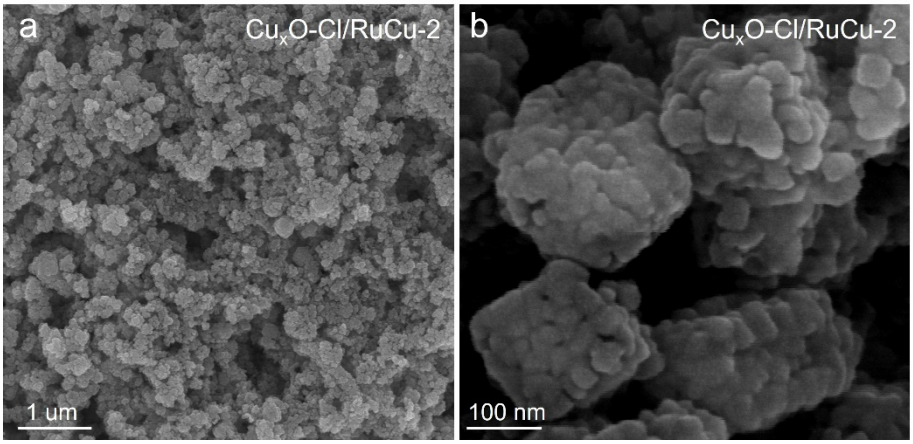

Fig. S5. SEM images of Cu_xO-Cl/RuCu-2

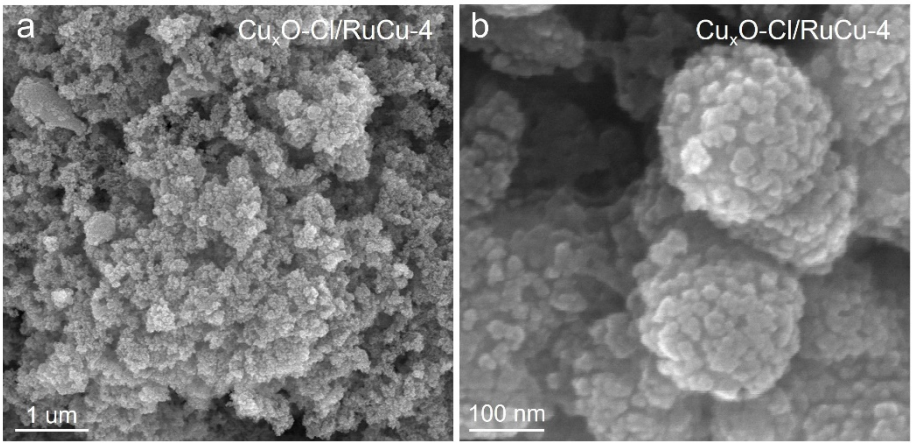

Fig. S6. SEM images of Cu_xO-Cl/RuCu-4

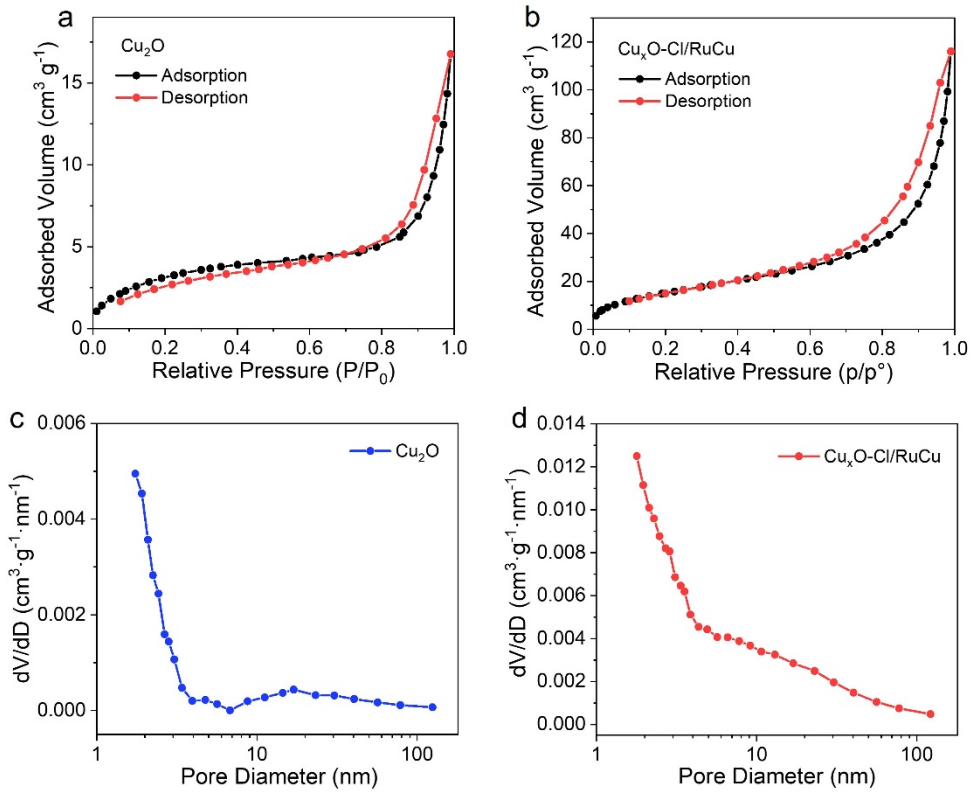

Fig. S7. Nitrogen adsorption-desorption isotherm of (a) Cu_2O and (b) Cu_xO-Cl/RuCu electrocatalysts. (c) The corresponding pore size distributions of (c) Cu_2O and (d) Cu_xO-Cl/RuCu electrocatalysts.

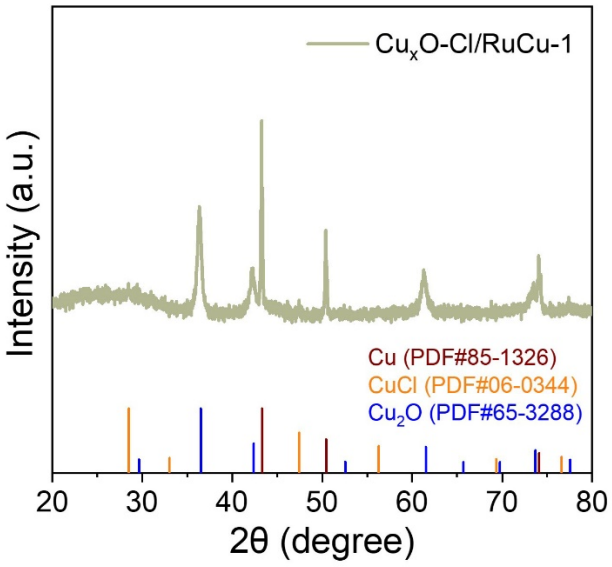

Fig. S8. XRD spectrum of Cu_xO-Cl/RuCu-1 powder

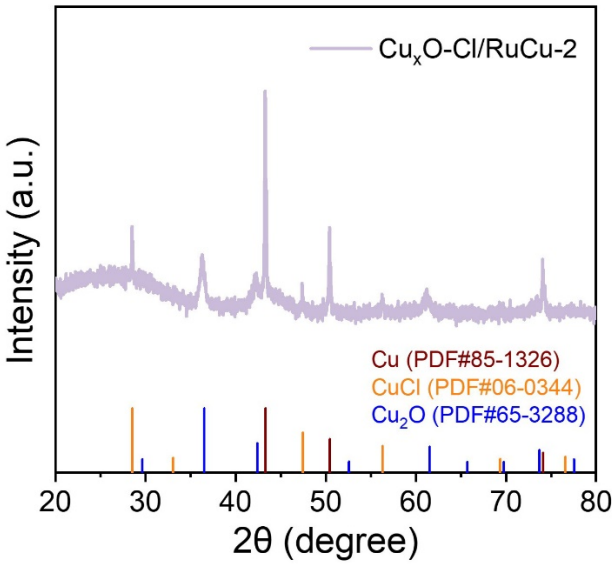

Fig. S9. XRD spectrum of Cu_xO-Cl/RuCu-2 powder

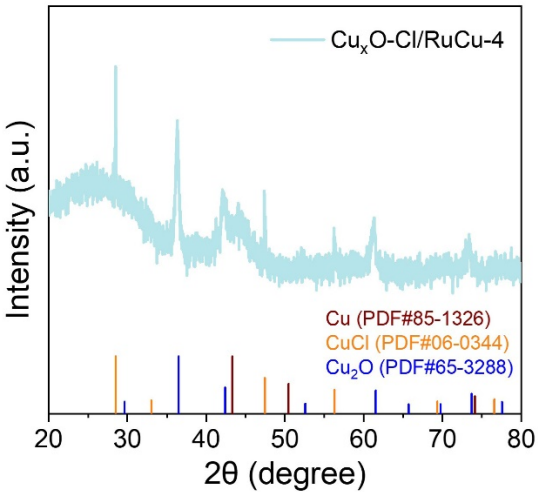

Fig. S10. XRD spectrum of Cu_xO-Cl/RuCu-4 powder

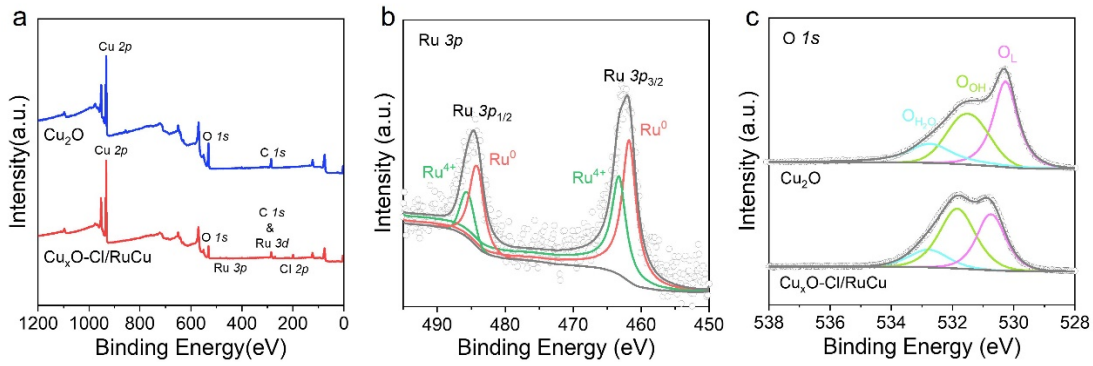

Fig. S11. (a) full XPS spectra for Cu_2O and Cu_xO-Cl/RuCu. High-resolution XPS spectra of (b) Ru 3p for Cu_xO-Cl/RuCu. (c) O 1s for Cu_2O and Cu_xO-Cl/RuCu

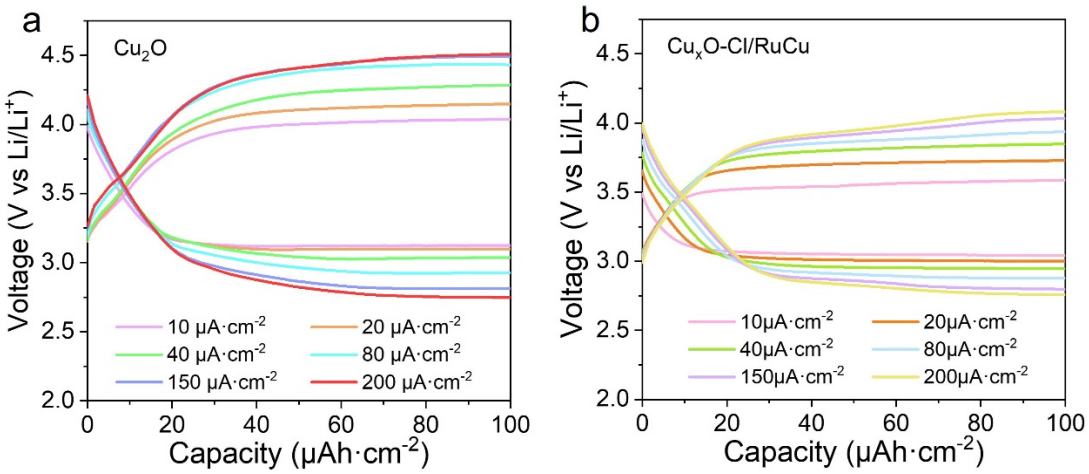

Fig. S12. Capacity-voltage curves of (a) Cu_2O and (b) Cu_xO-Cl/RuCu at different current densities

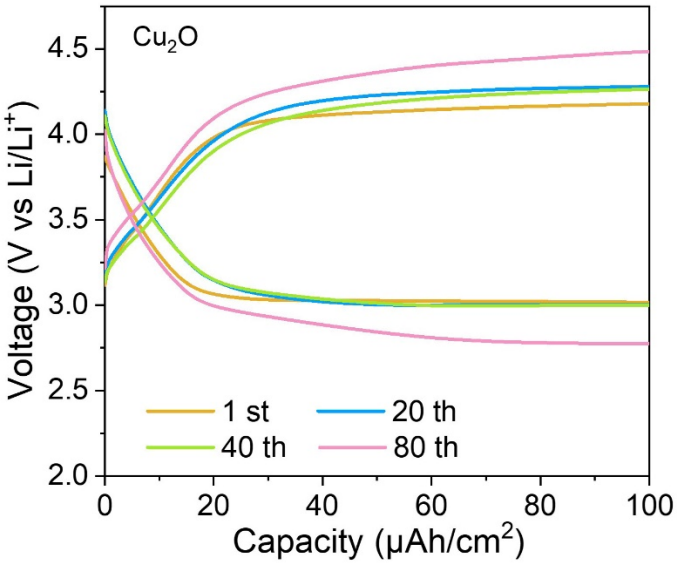

Fig. S13. Capacity-voltage curves of Cu_2O at different cycles

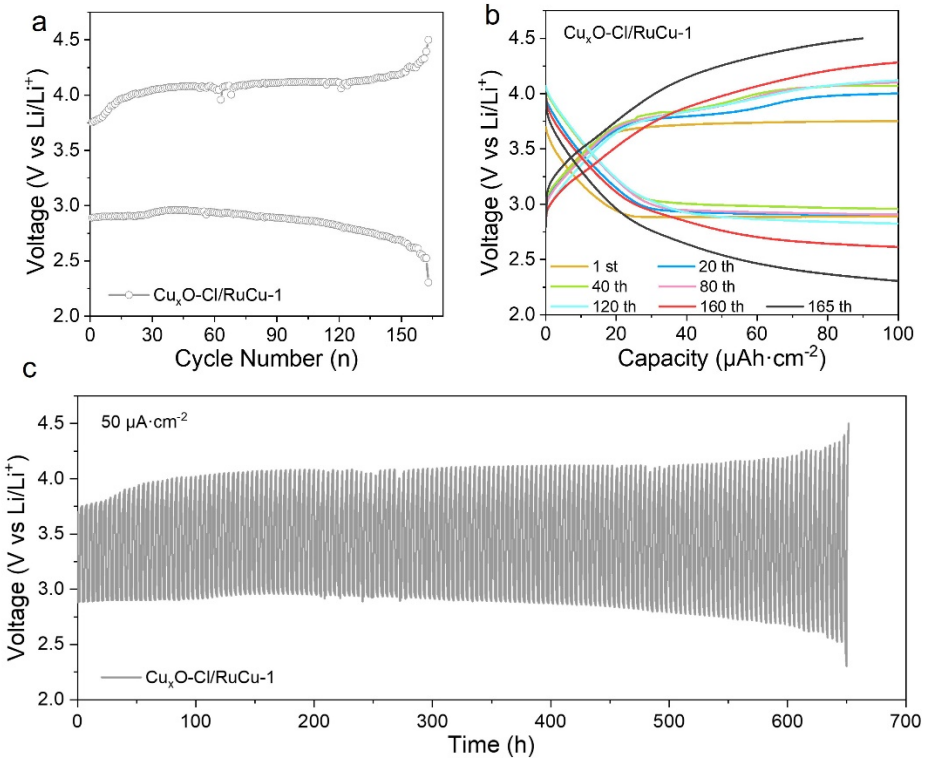

Fig. S14. Cycling performance diagram for Cu_xO-Cl/RuCu-1 electrocatalyst. (a) Charge-discharge cut-off voltage curves. (b) Capacity-voltage curves. (c) Time-voltage curve

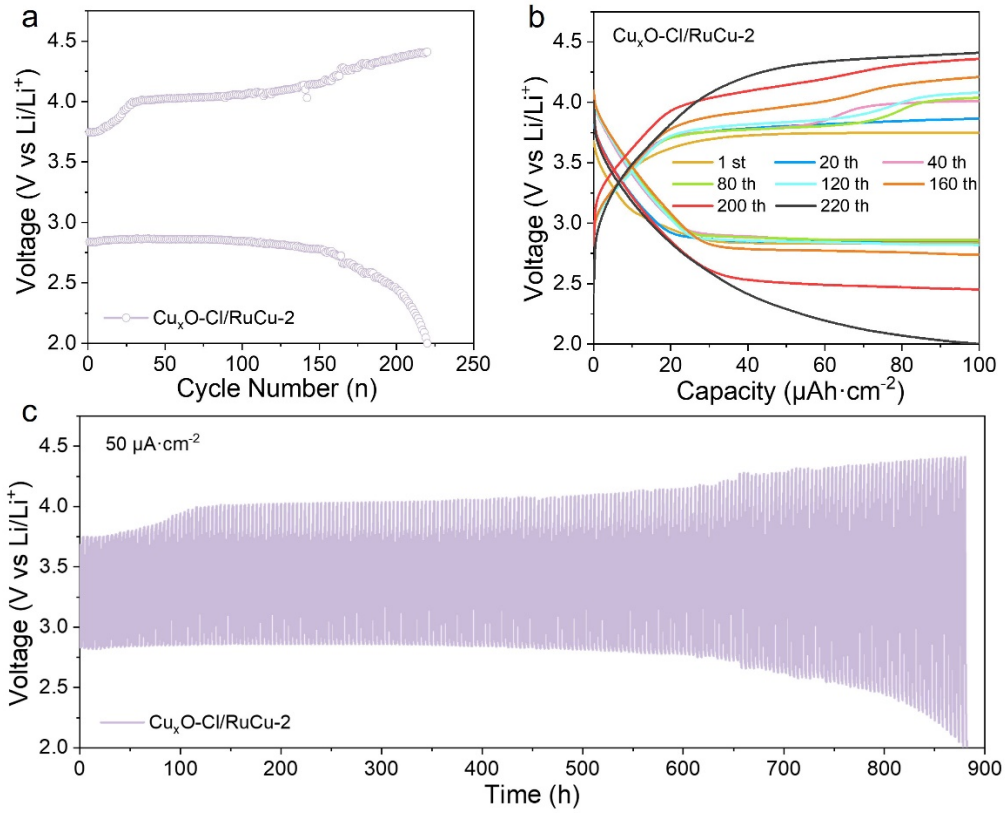

Fig. S15. Cycling performance diagram for Cu_xO-Cl/RuCu-2 electrocatalyst. (a) Charge-discharge cut-off voltage curves. (b) Capacity-voltage curves. (c) Time-voltage curve

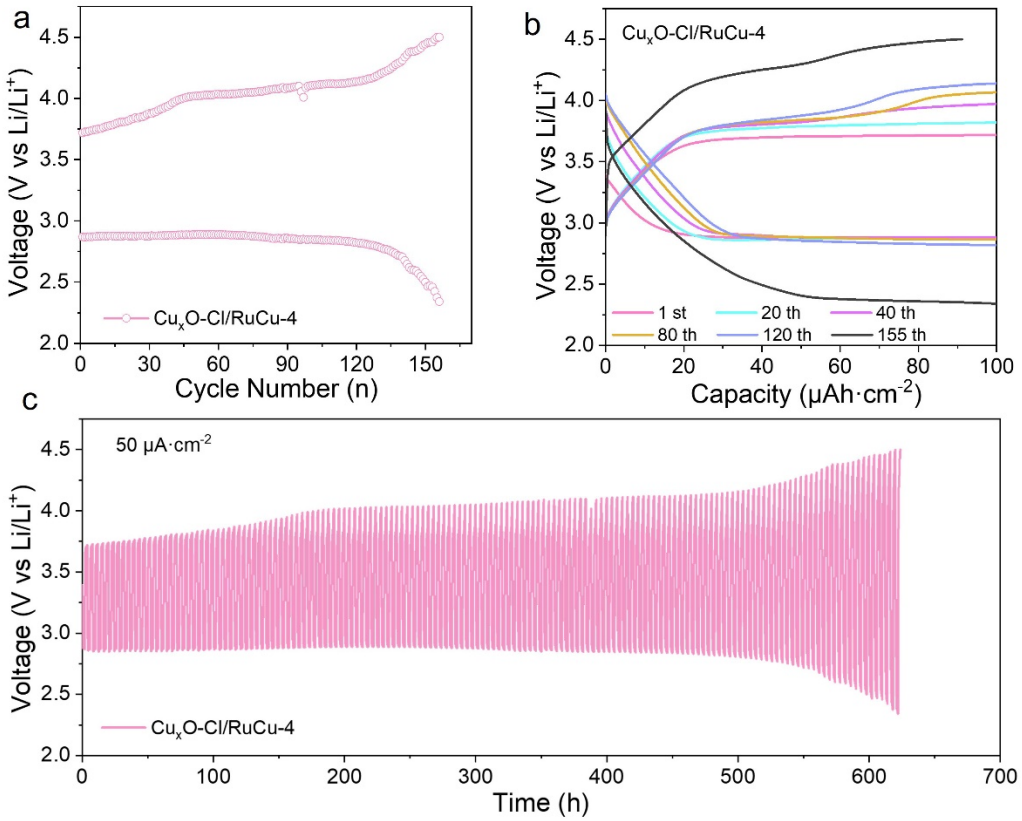

Fig. S16. Cycling performance diagram for Cu_xO-Cl/RuCu-4 electrocatalyst. (a) Charge-discharge cut-off voltage curves. (b) Capacity-voltage curves. (c) Time-voltage curve

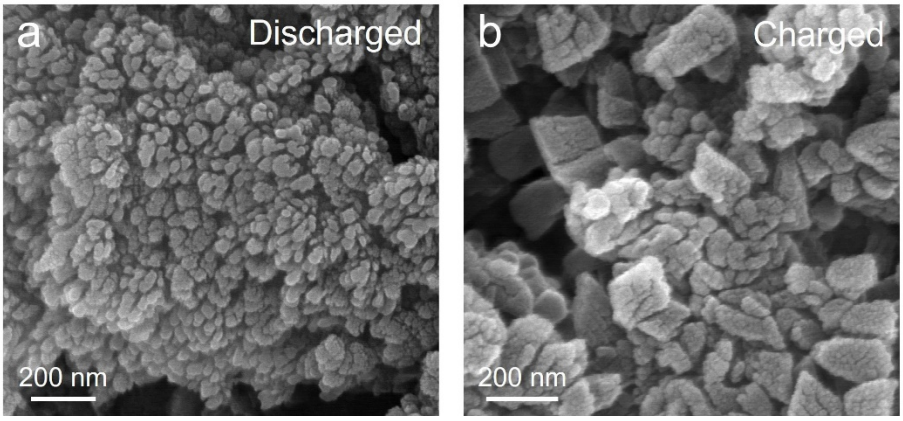

Fig. S17. SEM images of Cu_2O cathode after charge and discharge

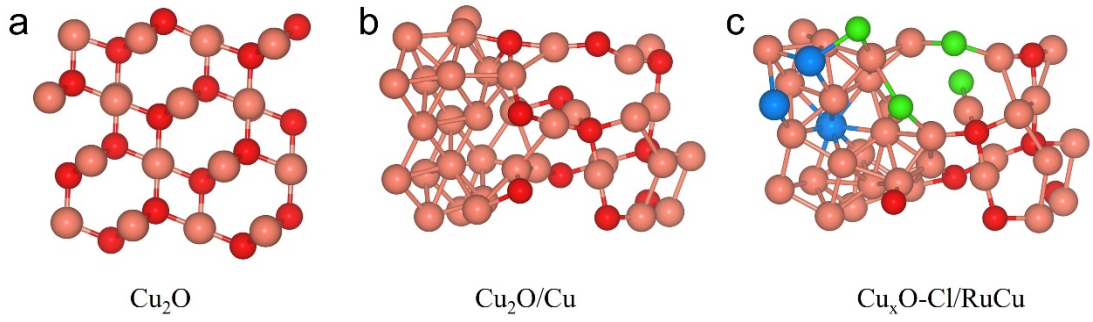

Fig. S18. The optimized structure for (a) Cu_2O, (b) Cu_2O/Cu and (c) Cu_xO-Cl/RuCu

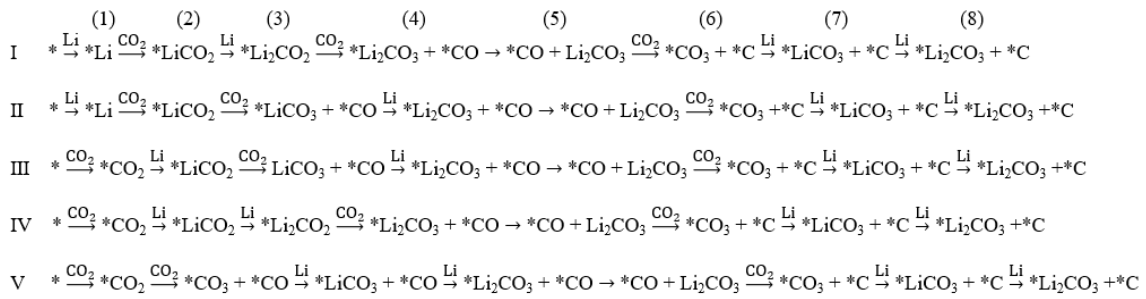

Fig. S19. Possible reaction pathways for the formation of Li_2CO_3 and C in the Li-CO_2 battery system of this work

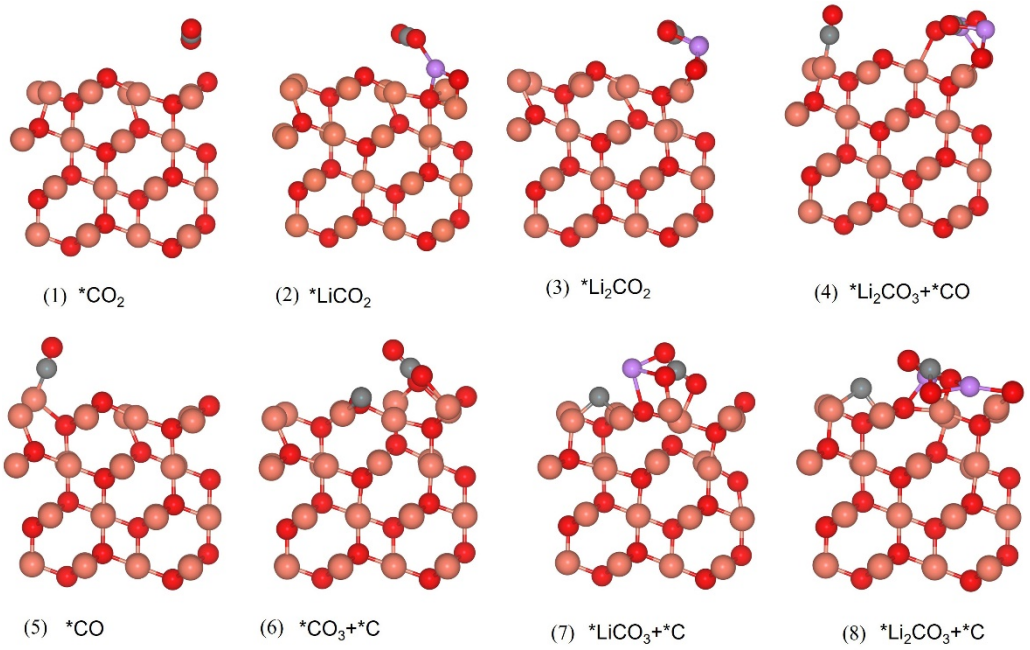

Fig. S20. The side views of adsorption configuration on Cu_2O

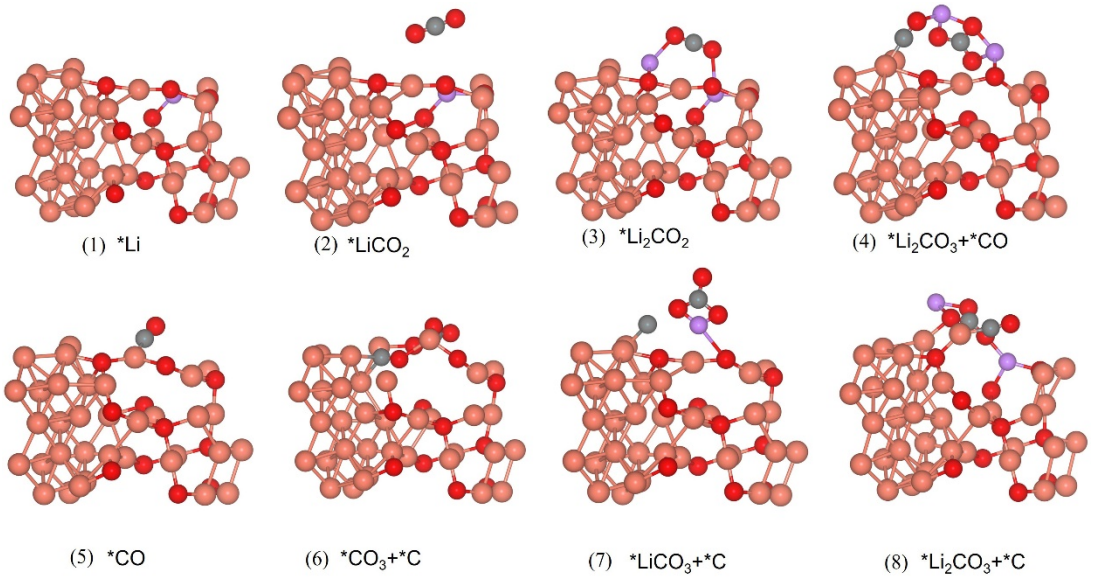

Fig. S21. The side views of adsorption configuration on Cu_2O/Cu

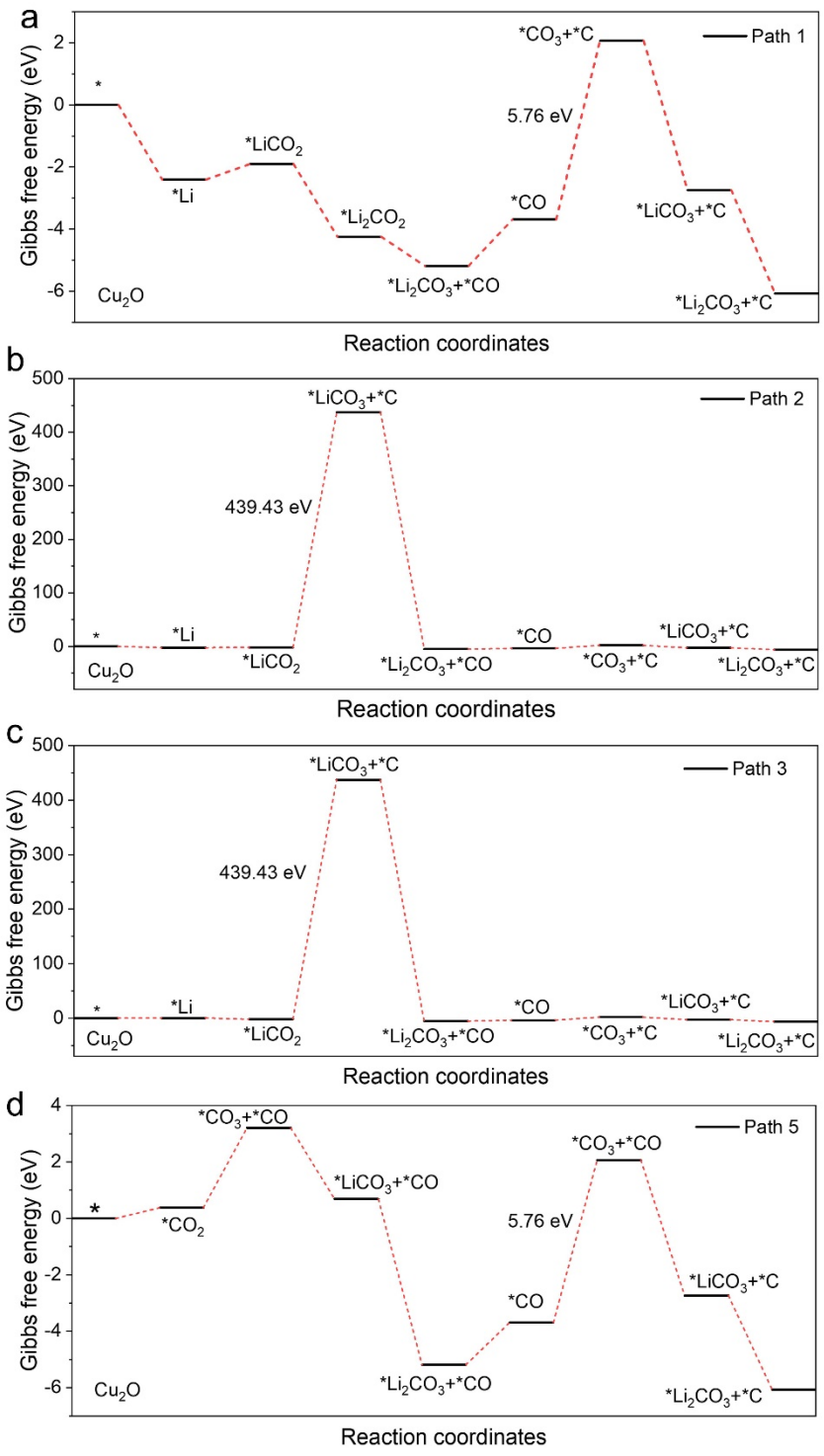

Fig. S22. The Calculated Gibbs free energy profiles for the nucleation of Li_2CO_3 and C on the surface of Cu_2O

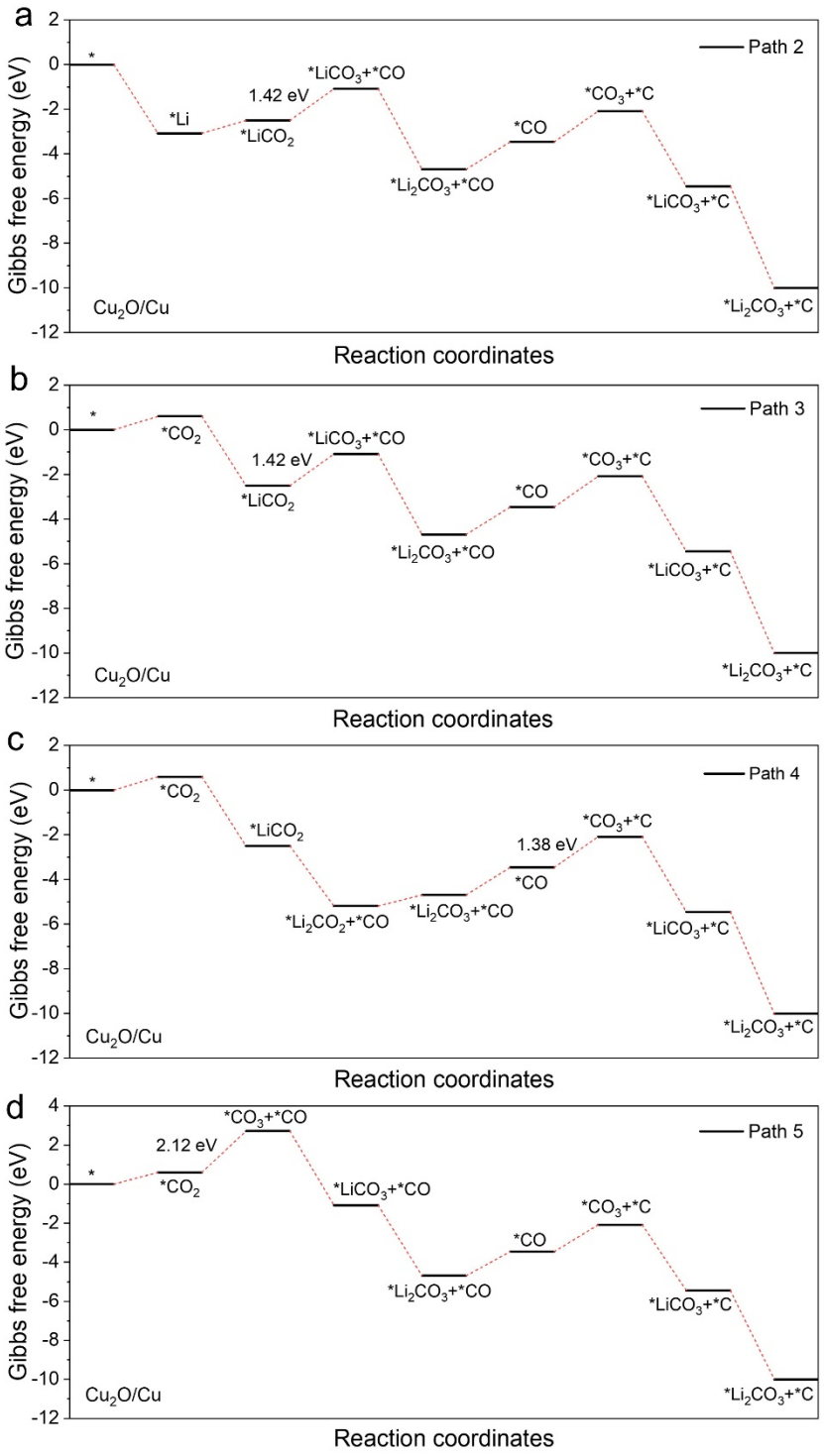

Fig. S23. The Calculated Gibbs free energy profiles for the nucleation of Li_2CO_3 and C on the surface of Cu_2O/Cu

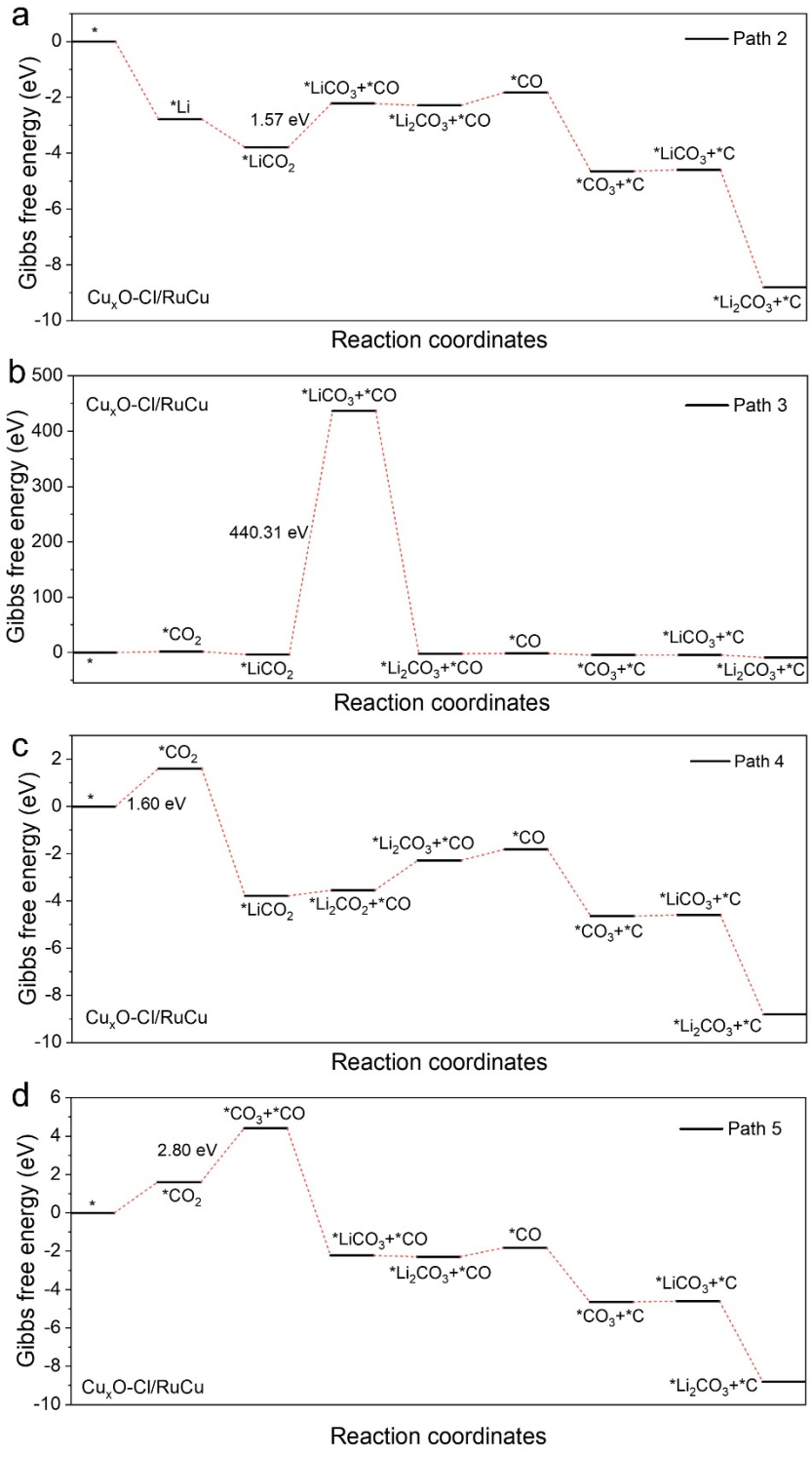

Fig. S24. The Calculated Gibbs free energy profiles for the nucleation of Li_2CO_3 and C on the surface of Cu_xO-Cl/RuCu

Table S1. The BET surface area and pore size for Cu_2O and Cu_xO-Cl/RuCu e lectrocatalysts

Electrocatalyst	BET Surface Area ($m^2 \cdot g^{-1}$)	Total Pore Volume ($cm^3 \cdot g^{-1}$)	Avg. Pore Diameter (nm)
Cu_2O	11.63	0.0253	8.7167
Cu_xO-Cl/RuCu	53.34	0.1774	13.3045

Table S2. The element ratio of Cu_xO-Cl/RuCu

Element	Atomic ratio (%)	Mass ratio (%)
O	25.85	7.50
Cu	57.41	66.14
Ru	13.12	24.04
Cl	3.62	2.33

Table S3. The comparison of Li-CO_2 battery electrocatalysts[S1-12]

Electrocatalyst	Overpotential	Charge Voltage	Cycling performance	Discharge capacity	Ref.
Cu_xO-Cl/RuCu	0.54 V	3.59 V	180 cycles at 50 μA·cm^{-2}	8041.73 μAh·cm^{-2} at 50 μA·cm^{-2}	This work
CoS-Vs-1.0	0.62 V	3.61 V	600 h at 20 μA·cm^{-2}	4637.6 μAh·cm^{-2} at 50 μA·cm^{-2}	S1
Cu-Co_3O_4	0.73 V	3.8 V	800 h at 20 μA·cm^{-2}	6950 μAh·cm^{-2} at 50 μA·cm^{-2}	S2
$CoSe_2$/CMF	0.72 V	3.86 V	162 cycles at 20 μA·cm^{-2}	5620 μAh·cm^{-2} at 50 μA·cm^{-2}	S3
V-MoS_2/Co_9S_8@CP	0.68 V	3.67 V	630 h at 20 μA·cm^{-2}	3954 μAh·cm^{-2} at 40 μA·cm^{-2}	S4
P-Mn_2O_3/KB	1.8 V	4.3 V	50 cycles at 50 mA·g^{-1}	9434 mAh·g^{-1} at 50 mA·g^{-1}	S5
N,S-doped CNTs	1.67 V	4.3 V	538 cycles at 200 mA·g^{-1}	23560 mAh·g^{-1} at 200 mA·g^{-1}	S6
Adjacent Co/GO	1.64 V	4.15 V	100 cycles at 100 mA·g^{-1}	17358 mAh·g^{-1} at 100 mA·g^{-1}	S7
Ru/ACNF	1.35 V	4.15 V	50 cycles at 100 mA·g^{-1}	11495 mAh·g^{-1} at 200 mA·g^{-1}	S8
Ru/NS-G	1.13 V	4.04 V	100 cycles at 100 mA·g^{-1}	12448 mAh·g^{-1} at 100 mA·g^{-1}	S9
B-NCNT	1.04 V	4.05 V	360 cycles at 1000 mA·g^{-1}	23 328 mAh·g^{-1} at 50 mA·g^{-1}	S10
$Co_{0.1}Ni_{0.9}O_x$/CNT	1.27 V	3.94 V	50 cycles at 100 mA·g^{-1}	5871 mAh·g^{-1} at 100 mA·g^{-1}	S11
Fe-ISA/N, S-HGs	1.17 V	3.95 V	200 cycles at 1000 mA·g^{-1}	23174 mAh·g^{-1} at 100 mA·g^{-1}	S12

References

S1 B. Lu, X. Wu, M. Zhang, X. Xiao, B. Chen, Y. Liu, R. Mao, Y. Song, X.-X. Zeng, J. Yang and G. Zhou, *J. Am. Chem. Soc.*, 2024, **146**, 20814-20822.

S2 J. Qiu, M. Wang, Y. Liu, Y. Song, Z. Yang, Y. Chen, B. Lu, X. Tao, J. Yang and G. Zhou, *Angew. Chem. Int. Ed.*, 2025, **n/a**, e202516978.

S3 K. Wang, L. Liu, D. Liu, Y. Wei, Y. Liu, X. Wang, A. S. Vasenko, M. Li, S. Ding, C. Xiao and H. Pan, *Small*, 2024, **20**, 2310530.

S4 B. Lu, B. Chen, D. Wang, C. Li, R. Gao, Y. Liu, R. Mao, J. Yang and G. Zhou, *Proc. NatI. Acad. Sci.*, 2023, **120**, e2216933120.

S5 W. Ma, S. Lu, X. Lei, X. Liu and Y. Ding, *J. Mater. Chem. A.*, 2018, **6**, 20829-20835.

S6 L. Song, C. Hu, Y. Xiao, J. He, Y. Lin, J. W. Connell and L. Dai, *Nano Energ.*, 2020, **71**, 104595.

S7 B.-W. Zhang, Y. Jiao, D.-L. Chao, C. Ye, Y.-X. Wang, K. Davey, H.-K. Liu, S.-X. Dou and S.-Z. Qiao, *Adv. Funct. Mater.*, 2019, **29**, 1904206.

S8 Y. Qiao, S. Xu, Y. Liu, J. Dai, H. Xie, Y. Yao, X. Mu, C. Chen, D. J. Kline, E. M. Hitz, B. Liu, J. Song, P. He, M. R. Zachariah and L. Hu, *Energy Environ. Sci.*, 2019, **12**, 1100-1107.

S9 Y. Qiao, J. Wu, J. Zhao, Q. Li, P. Zhang, C. Hao, X. Liu, S. Yang and Y. Liu, *Energy Storage Mater.*, 2020, **27**, 133-139.

S10 X. Li, J. Zhou, J. Zhang, M. Li, X. Bi, T. Liu, T. He, J. Cheng, F. Zhang, Y. Li, X. Mu, J. Lu and B. Wang, *Adv. Mater.*, 2019, **31**, 1903852.

S11 X. Xiao, Z. Zhang, W. Yu, W. Shang, Y. Ma, X. Zhu and P. Tan, *ACS Appl. Energy Mater.*, 2021, **4**, 11858-11866.

S12 C. Hu, L. Gong, Y. Xiao, Y. Yuan, N. M. Bedford, Z. Xia, L. Ma, T. Wu, Y. Lin, J. W. Connell, R. Shahbazian-Yassar, J. Lu, K. Amine and L. Dai, *Adv. Mater.*, 2020, **32**, 1907436.